Degradation of malachite green dye by capping polyvinylpyrrolidone and *Azadirachta indica* in hematite phase of Ni doped Fe_2O_3 nanoparticles via co-precipitation method

Article history:
Received: 15-10-2022
Revised: 24-01-2023
Accepted: 01-02-2023

Naveen Thakur[a], Pankaj Kumar[b],
Ashwani Tapwal[c], Kamal Jeet[d]

Abstract: In the present research, a chemical co-precipitation approach has been used to approach the synthesis, characterization, and photocatalytic applicability of Ni-doped α-Fe_2O_3 (hematite) nanoparticles. Biosynthesized iron oxide nanoparticles (IONPs) were successfully synthesized using a non-toxic leaf extract of the *Azadirachta indica* (AI) plant (neem) as a reducing and stabilizing agent. X-ray diffraction (XRD), transmission electron microscopy (TEM), scanning electron microscopy (SEM), Raman spectroscopy, FT-IR spectroscopy, ultraviolet-visible (UV-Vis) spectroscopy, and vibrating sample magnetometer (VSM) have all been used to examine the synthesized materials. All of the produced NPs contain only the nanocrystalline hematite phase, according to XRD measurements. The morphology studies of the Ni-doping hematite nanoparticles, as demonstrated by TEM and SEM. The phase purity and phonon modes of the prepared nanoparticles are confirmed by Raman spectroscopy. The UV-Vis absorption tests show also that value of the band gap increases together with the reduction in particle size, going from 2.26 eV for chemical α-Fe_2O_3 to 2.5 eV for green Ni-doped α-Fe_2O_3 nanoparticles. Additionally, it was clear from the magnetic characteristics that all of the samples behaved ferromagnetically at ambient temperatures. On the other side, malachite green (MG) dye was used as a surrogate industrial wastewater dye in order to study the photocatalytic efficiency of Ni-doped α-Fe_2O_3 particles. The pure/green Ni-doped α-Fe_2O_3 NPs showed that after 70 minutes of exposure, 92% of the MG had become discolored.

Keywords: *Azadirachta indica;* Polyvinylpyrrolidone; Hematite.

1. INTRODUCTION

The creative and advantageous features of materials at the nanoscale have led to a steady expansion in research and commercial development in the field of nanotechnology today (Anu, Thakur & Kumar, 2018; Anu *et al.*, 2020; Balkrishna *et al.*, 2021a). Additionally, nanotechnology is a versatile technique that can be used to create catalysts, antimicrobial coatings, electrical devices, and manufacturing techniques (Lalitha, Subbaiya, & Ponmurugan 2013; Ramasamy, Mohana, & Suresh 2017). Millions of contaminants are released into water sources as a result of the population's rapid growth and industrial activity, making pollution and water scarcity major problems.

[a] Department of Physics, Career Point University, Hamirpur, Himachal Pradesh, 176041, India. Center for Nano-Science and Technology, Career Point University, Hamirpur, Himachal Pradesh, 176041, India.
Corresponding author: naveenthakur2327@gmail.com

[b] Department of Physics, Career Point University, Hamirpur, Himachal Pradesh, 176041, India. Center for Nano-Science and Technology, Career Point University, Hamirpur, Himachal Pradesh, 176041, India.

[c] Himalayan Forest Research Institute, Shimla, Himachal Pradesh-171009, India.

[d] Department of Pharmaceutical Sciences, Career Point University, Hamirpur, Himachal Pradesh 176041, India.

https://doi.org/10.37819/nanofab.008.304

Because of the increasing harm, it causes to the security of the water supply, health impacts, ecological processes, and essentially the quality of life, this needs to be resolved (Balkrishan *et al.*, 2021b; Khatana *et al.*, 2021; Patial and Thakur, 2018). Since water is the source of all life, addressing the serious problem of water pollution is crucial if we are to ensure that there is enough clean water to meet the needs of humans, other living things, and economic enterprises (Thakur *et al.*, 2023a; Thakur, Thakur & Kumar, 2023b). Biohazardous material and toxic water pollution-related environmental issues have garnered a lot of awareness (Sharma *et al.*, 2020b; Sharma *et al.*, 2021c; Thakur, Anu & Kumar, 2020). One of the main categories of contaminants in wastewater discharged from textile and other industrial activities is organic dyes (Thakur *et al.*, 2021a; Thakur *et al.*, 2022a). These non-destructive chemical and biological procedures for the remediation of pollutants essentially convert the non-biodegradable material into sludge, creating a new sort of pollution that requires additional processing (Ahmed *et al.*, 2021; Kumar *et al.*, 2022a; Kumar *et al.*, 2020a). From the triphenylmethane family, malachite green (MG) is one of the most common water-soluble dyes. It is extensively utilized in a variety of sectors, including those that produce food, textiles, paper, plastic, cosmetics, pharmaceuticals, and medical industries (Cheng *et al.*, 2022; Adegoke *et al.*, 2022; Mahmoud, El-Sharkawy, & Ibrahim 2022; Wu *et al.*, 2022). Unfortunately, the high quantities of MG produced in the aqueous solution cause living things to suffocate and also have mutagenic, teratogenic, and carcinogenic toxicity consequences for humans (Sharma and Kumar, 2021a; Sharma, Kumar & Thakur, 2021b; Sharma *et al.*, 2020a).

Therefore, removing chemical constituents and MG from water has always been a focus of environmental research in an effort to lessen the negative impacts of these substances on both humans and the environment (Thakur *et al.*, 2021b; Thakur *et al.*, 2022b). There are a number of ways to get rid of this pollutant, but adsorption is one of the most prevalent because it doesn’t produce any secondary pollution, is effective at getting rid of the pollutant, and is also cost-effective (Sogut *et al.*, 2022; Kumar *et al.*, 2023a; Kumar *et al.*, 2020b). Iron oxides have been employed as adsorbents by numerous researchers. The present research concentrates on using IONPs (hematite) as adsorbents to remove MG and phenol from an aqueous in this approach (Bonyadi, Khatibi, & Alipour 2022; Mostafa, & Amdeha 2022). The ferromagnetic behavior of nickel-doped hematite NPs has recently been demonstrated in experimental research on their manufacture and characterization (Bustamante-Torres *et al.*, 2022). The observation may correlate saturation magnetization with nickel concentration; however, the increase or decrease in coercivity requires additional analysis (Lu *et al.*, 2022). Because Ni^{2+} and Fe^{3+} have comparable ionic radii (0.69 and 0.64, respectively), Ni^{2+} can accommodate Fe^{3+} in the crystal structure of hematite NPs, which is another utility of doping with Ni.

Alternatively, an iron oxide precursor should always be oxidized in order to complete the formulation. IONPs have been created using a variety of techniques, including thermal reactions, electrochemical processes, microemulsion, sol-gel, co-precipitation, and so on (Yakasai *et al.*, 2022; Jabbar, Barzinjy, & Hamad 2022; Prakash *et al.*, 2022). The co-precipitation process is adaptable, and affordable resulting in excellent product yields, reducing contamination and utilizing lesser solvents (Singh, Singh, & Gupta 2022).

Doping of these metals is liable for raising the saturation magnetization of the metal oxide-based NPs. We selected Ni for the doping because, in contrast to certain other transition metals, Ni-doped NPs demonstrate super magnetic properties at ambient temperature (Moharana, Kumar, & Kumar, 2020). The dopant nickel is highly magnetic and ferromagnetic in nature. The possibility of creating ferromagnetism in nickel-based ferromagnetic semiconductors is also supported by certain theoretical research (Grabsi *et al.*, 2022). Thus, it is obvious that Ni can have a significant impact on the magnetic characteristics of hematite NPs. The purpose of this research is to utilize an extract from the leaves of *Azadirachta indica* (AI) (often referred to as neem), a plant belonging to the mahogany family Meliaceae, to create IONPs in a sustainable manner. Since earlier civilizations, this plant has been used as medicine to treat bacterial, fungal, viral, and numerous other skin conditions. The two significant phytochemicals in neem, terpenoids, and flavanones, are essential for stabilizing the nanoparticle and performing as capping and reducing agents (Maji, 2021; Ujah *et al.*, 2021). The main objectives of this research are to fabricate and analyze the photocatalytic efficiency of nano iron oxide by use of the co-precipitation method or catalysis to prevent any pollution. The precipitants’ implications on Ni-doped hematite NPs are also being analyzed. Malachite Green (MG) photodegradation is observed in an aqueous solution when exposed to ultraviolet (UV) light. The degradation efficiency of pure/green synthesized was also assessed for comparison purposes.

2. MATERIALS AND METHODS

2.1. Materials

Chemical	Chemical Formula	Molecular Mass (g/mol)	Supplier	Purity (%)
Iron (III) Chloride Hexahydrate	$FeCl_3.6H_2O$	270.33	Sigma Aldrich	97
Nickel (II) chloride hexahydrate	$NiCl_2.6H_2O$	237. 7	EMPLURA	97
Polyvinylpyrrolidone (PVP)	$(C_6H_9NO)_n$	1,300,000	Sigma Aldrich	—
Sodium Hydroxide	NaOH	39.997	Merck	97
Malachite green	$C_{23}H_{25}N_2Cl$	364.92	Sigma-Aldrich	>98

Table 1. List of the chemical with specification that were employed.

2.2. Preparation of *Azadirachta indica* (Neem) leaf extracts

Azadirachta indica trees in the Himachal Pradesh area of Hamirpur were harvested for their fresh leaves. To properly clean the dust and debris from the leaves surface, they were extensively washed under running water. 100 ml of double-distilled water goes combined with 20 g of finely chopped neem leaves, and the combination was heated for 30 minutes until the color of the aqueous solution varied from clear to dark brown. The extract was filtered with filter paper after being cooled to ambient temperature. To be used for further experimentation, the extract was kept in a refrigerator.

2.3. Synthesis of Ni-doped Fe_2O_3 NPs

The co-precipitation approach was utilized to manufacture Ni-Fe_2O_4 superparamagnetic nanoparticles from ferric chloride hexahydrate ($FeCl_3.6H_2O$, nickel chloride hexahydrate ($NiCl_2.H_2O$), and sodium hydroxide (NaOH). Firstly, the solution of $NiCl_2.H_2O$ was prepared in distilled water and stirred for 1 hour at 60 ºC just about. Then the solution of $FeCl_3.6H_2O$ was prepared in the distilled water and stirred for 1 hour at 60 ºC. Subsequently, solutions of $NiCl_2.H_2O$ and $FeCl_3.6H_2O$ were mixed with continuous stirring at 80 ºC. As a capping agent and surfactant, polyvinylpyrrolidone (PVP)/plant extract was utilized. Then, drop by drop, NaOH was added until the pH reached 11. The precipitate was washed with distilled water and ethanol before drying for 8 hours in an oven at 80 ºC. The prepared fine powder is calcined at 700 ºC with a gradient of 10 ºC/min for 3 hours, then cooled with the same gradient. The samples are then gathered and put to use in future investigations. Eq. 1 has been used to describe the Ni-Fe_2O_3NPs chemical process.

$$2Fe_3^{+} + Ni_2^{+} + 8OH^{-1} \rightarrow NiFe_2O_3 + 4H_2O \quad (1)$$

2.4. Measurement of Photocatalytic activity

A study using photocatalysis was carried out in a specially built reactor that also has a magnetic stirrer and a UV lamp. Under the illumination of a 125 W (UV-C, 254 nm) Mercury lamp (Phillips), the photocatalytic activities of pure/green synthesized Ni-doped hematite NPs toward the degradation of malachite green (MG) dye solution were analyzed. In a conventional test, 10 mg of the photocatalyst was added to 100 ml of dye solution. After being in the dark for an hour to reach adsorption characteristics, it was exposed to UV radiation. After regular intervals of 7 minutes, approximately 5 ml of the irradiated solutions were removed, and the solution's absorption spectra were determined to track the photocatalytic activity.

3. RESULTS AND DISCUSSION

3.1. Structural analysis

The X-ray diffractometer was used to analyze Ni-doped hematite NPs using Kα_1 radiation with a wavelength of λ = 1.54 Å as a targeted source of X-ray preparation. The nanoparticle sample was analyzed at a scanning speed of 0.02°/min, step size of 0.031°, and step time of 0.3 sec in the angle range of 2θ. As shown in Fig. 1, powder samples of pure /green Ni-doped hematite NPs revealed their crystalline structure. According to (JCPDS card No. 01-078-6916) (Plachtova, *et al.*, 2018), all of the observed peaks may be indexed in accordance with the predicted rhombohedral (hexagonal) structure of chemical/green hematite NPs (space group: R-3c) with lattice parameters. All of the prepared samples' diffracting peaks were shown in Fig. 1 at 2θ range of pure 24.28°, 31.79°, 33.35°, 35.73°, 41.04°, 45.53°, 49.56°, 54.23°, 57.80° 62.75°and 64.12° with miller indices (012) (220), (104), (110), (113), (111), (024), (116) (018) (214) and (300) and green 24.37°, 31.98°, 33.26°, 35.83°, 41.06°, 45.62°, 49.65°, 54.21°, 57.61°, 62.74°and 64.10° with miller indices (012) (220), (104), (110), (113), (111), (024), (116) (018) (214) and (300) respectively.

The formula shown below was used to get the lattice parameter:

$$a = d_{hkl}\sqrt{h^2 k^2 l^2} \qquad (2)$$

$$n\lambda = 2d \sin \theta C \qquad (3)$$

The equation below was utilized to determine crystallite size:

$$D = \frac{\cos K X \lambda}{\beta \cos \theta} \qquad (4)$$

Where D is the crystallite size of the diffraction peak, K represents the shape component of the particles which is 0.9, λ is the wavelength of the radiation has the value 1.54 Å, β is the full width at half maxima of the diffraction peak, and θ is the corresponding Bragg's diffraction angle. The crystallite size of pure/green Ni-doped hematite NPs was calculated using the (104) plane.

The dislocation density (δ) was calculated according to the relation, where is the length of the dislocation lines per unit volume of the crystal.

$$\delta = \frac{1}{D_2} \, lines / m^2 \qquad (5)$$

Sample	Fe_2O_3 NPs	Crystallite Size (D) (nm)	Interplanar spacing (d) (Å)	Lattice Parameters (Å) a = b, c Hematite		Volume (V)	Dislocation Density (δ) (nm^{-2})	Strain (ε)
Chemical	Hematite	19.4202	2.68346	5.04	13.62	277.136	0.002651	0.006184
Green	Hematite	13.8577	2.69051	5.10	13.73	191.822	0.005213	0.009095

Table 2. Lattice characteristics, crystallite sizes, dislocation density, and micro-strain.

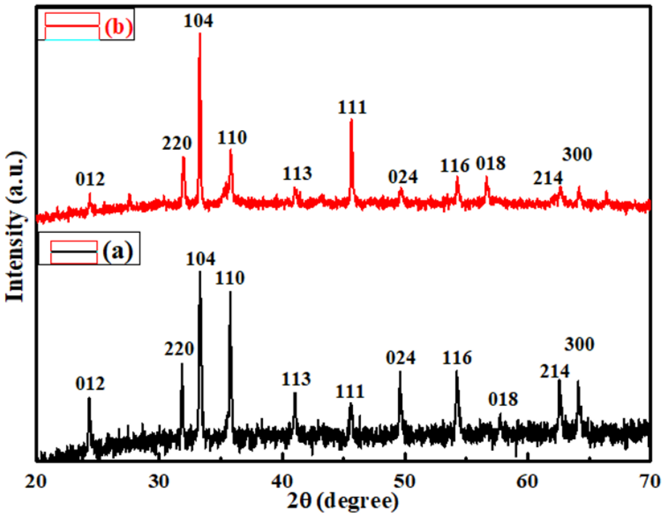

Figure 1. XRD pattern of hematite crystal lattices of (a) chemical Ni-doped hematite (α-Fe_2O_3) and (b) green Ni-doped hematite (α-Fe_2O_3) NPs.

Additionally, as Ni-doping gives the opportunity, the (104) diffraction peak's intensity gradually decreases, and its half-height width increases. The decrease in peak intensity when nickel is doped into hematite can be explained by the fact that Ni behaves as nucleation nuclei for the production of crystalline grains. This is consistent with a decrease in grain relative size to the pure sample as indicated by an increase in the half-height width of the diffraction peaks. The variation of average crystallite sizes obtained in the XRD data has 13-19 nm. As a result, it is seen that green Ni-doped hematite NPs size decreases due to an increase in nucleation center density in the doped samples.

3.2. Chemical composition analysis

Raman spectra of green Ni-doped hematite NPs were obtained at ambient temperature at excitation wavelengths of 624.04 nm as shown in Fig. 2. Hematite NPs since it belongs to the R-3c crystal space group and consequently six phonon lines are predicted to arise in the Raman spectrum, in particular two A1g phonon modes and four Eg phonon modes in the table (2). The Ni-doped hematite NPs were completely in the hematite phase as a result, and all Raman characteristics intensified with Ni substances. These increases in Raman peak intensity could be attributed to the symmetry breaking of the hematite lattice brought on by the addition of green synthesis. All phonon modes became more intense after doping hematite NPs. Additionally, after green doping, the virtually intense chemical/doping Eg Raman band at 288 cm^{-1} broadens and shifts toward the higher wave number of green/doping 292 cm^{-1}. With hematite NPs, comparable outcomes have been reported (Testa-Anta, *et al.*, 2019); Nyarige, Kruger, & Dialen 2020).

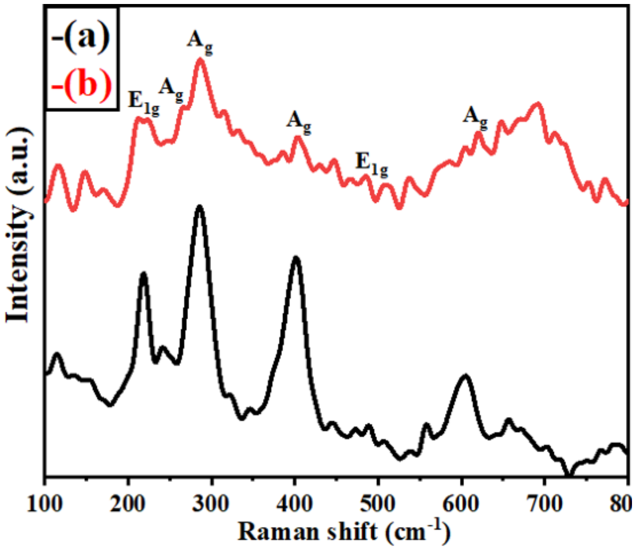

Figure 2. Raman Spectra of SEM images of hematite crystal lattices of (a) Chemical Ni-doped hematite (α-Fe_2O_3) and (b) Green Ni-doped hematite (α-Fe_2O_3) NPs.

Chemical Hematite		Green Hematite	
Peaks (cm^{-1})	Modes	Peaks (cm^{-1})	Modes
220	A1g	222	A1g
244	Eg	245	Eg
288	Eg	292	Eg
408	Eg	410	Eg
491	A1g	491	A1g
609	Eg	610	Eg

Table 3. Raman peaks that corresponded to the hematite NPs' synthesized modes.

3.3. Optical Analysis

Analysis of the UV-Vis absorption spectra of pure/green Ni doped hematite NPs, all of which exhibit absorption curves in the range between 200 and 800 nm in shown in Fig. 3. In sample (a), pure Ni-doped hematite NPs show high absorption at wavelengths of 546 nm, and in sample (b), green Ni-doped hematite NPs show excessive absorption at wavelengths of 496 nm. Although nanoparticles may be anticipated due to the reduction in particle size caused by doping, a little reduction in the absorption edge similar to that shown in Ni in hematite NPs was also seen.

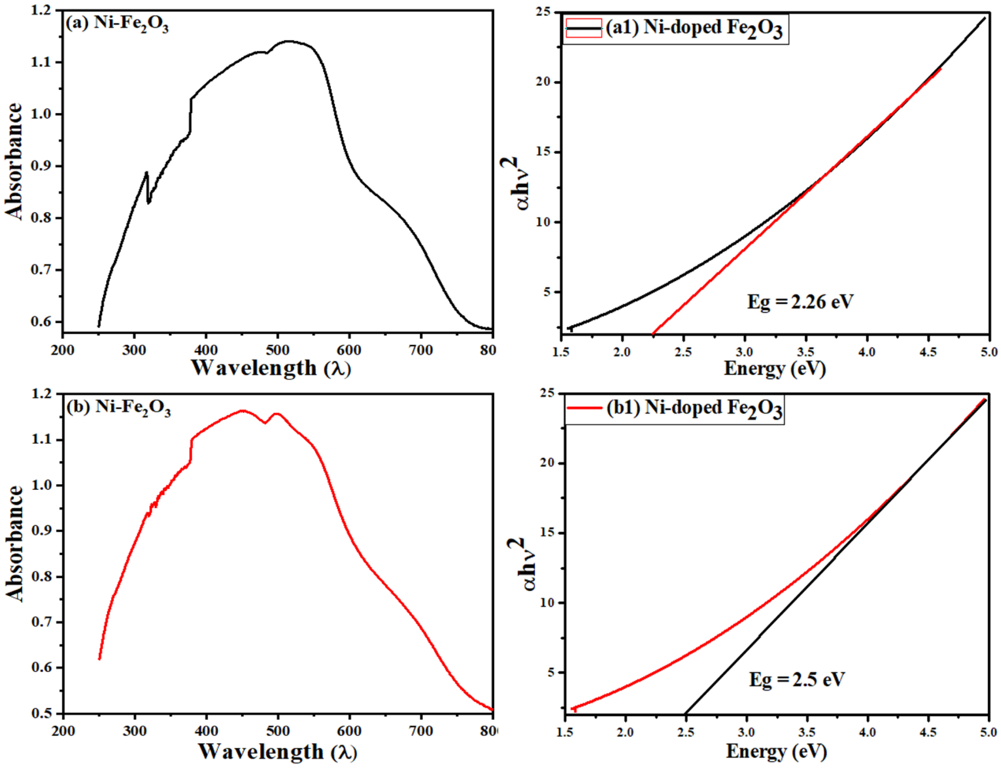

Figure 3. UV-Analysis and band gap of (a,a1) chemical Ni-doped hematite (α-Fe_2O_3) and (b,b1) Green Ni-doped hematite (α-Fe_2O_3) NPs.

A straight band gap (n = 2) exists in hematite NPs. One of the crucial methods for determining the energy band gap of nanoparticles is UV-Visible absorption spectroscopy calculated from Eq. 6.

$$E = hc / \lambda \tag{6}$$

where c is the speed of light, E is the band gap energy, h is the plank's constant, and λ is the wavelength of the absorption edge. Using the formula, one might determine the value of

$$\alpha = (2.303 * A) / t \tag{7}$$

when α is absorption coefficient, A is absorbance coefficient of UV-Vis spectroscopy. Then, we determined hν.

$$\nu = c / \lambda \tag{8}$$

The desired value of the optical band gap was determined from the graph that was plotted between (αhν)1/2 on the y-axis and (hν) on the x-axis. The optical band gap of chemical/green Ni-doped hematite NPs increased from 2.27 to 2.5 eV as shown in Fig. 3 (a1,b1).

3.4. FT-IR spectroscopy

The presence of functional groups absorbed on the surface of synthesized particles by the co-precipitation approach was determined using FT-IR spectroscopy. The FT-IR spectra of pure/green Ni-doped hematite NPs that were calcined at 700 ºC are shown in Figure 4. It was possible to see the distinctive bands at 3428, 1633, 564, and 449 cm^{-1}. In the region of 3428 cm^{-1} and 1633 cm^{-1}, the absorption band attributed to the stretching and bending vibration of the water molecule is visible, and the bands of 564 cm^{-1} and 449 cm^{-1} are caused by the presence of Ni and the Fe-O vibrational mode of hematite NPs, which are responsible for the hematite phase in the rhombohedral lattice.

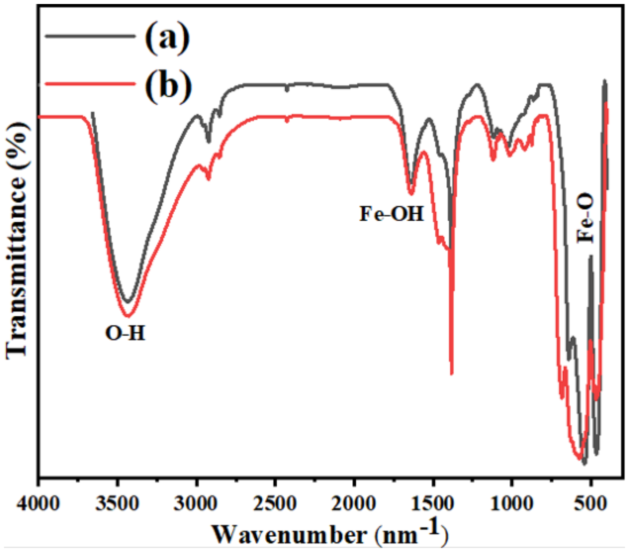

Figure 4. FTIR image of (a) chemical Ni-doped hematite (α-Fe_2O_3) and (b) Green Ni-doped hematite (α-Fe_2O_3) NPs.

3.5. Morphology and elemental composition analysis

SEM was used to analyze the surface morphology of the nanoparticles synthesized pure/green Ni-doped hematite nanoparticles. The crystallites of our samples pure/green Ni-doped hematite displayed fine, spherical shape and narrow size distribution, according to microscopic measurements of our samples Fig. 5 (a,b). The SEM images also show that the crystal structure grew smoother as a result of higher green Ni doping, and that the

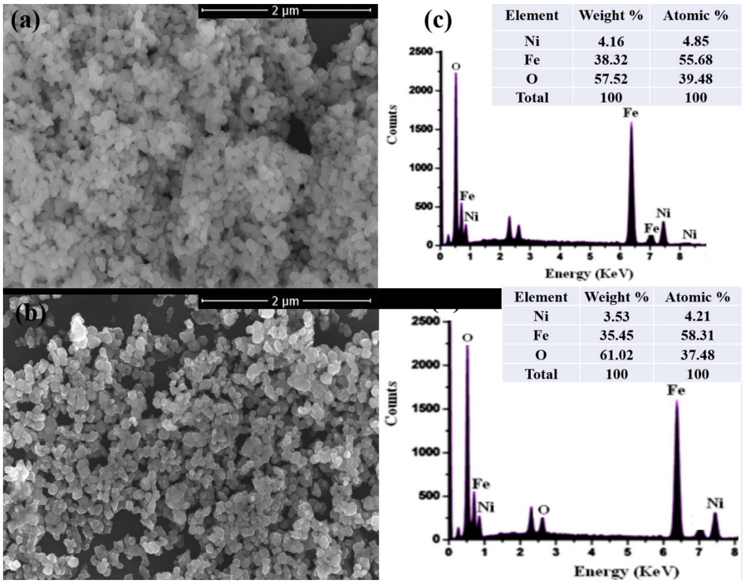

Element	Weight %	Atomic %
Ni	4.16	4.85
Fe	38.32	55.68
O	57.52	39.48
Total	100	100

Element	Weight %	Atomic %
Ni	3.53	4.21
Fe	35.45	58.31
O	61.02	37.48
Total	100	100

Figure 5. SEM & EDS images of crystal lattices of (a,c) chemical Ni-doped hematite (α-Fe_2O_3) and (b,d) Green Ni-doped hematite (α-Fe_2O_3) NPs.

orientation of the microparticles was dependent on the amount of Ni-doped iron oxide. The XRD discussion also comes to the same conclusion. Iron (Fe), Nickel (Ni), and Oxygen (O) were revealed in the EDX spectrum of pure/green Ni-doped hematite (Fig. 5 c,d).

The surface morphology of pure/green Ni doped hematite (calcined at 700 oC) both formed spherical nanoparticles, according to TEM examinations Fig. 6 (a,b). The size of the particles, which were found to be monodispersed and to have a limited size range, was noted to be ~18 nm for pure particles and ~11 nm for green Ni-doped hematite NPs. It’s interesting that no hematite nanoparticle aggregation was seen, and the 11 nm attributed crystallites formed a spontaneous system. Therefore, it may be concluded that Ni-doping can undoubtedly stop the development of nanosized hematite particles. The small size of the hematite NPs is confirmed by TEM studies, and the measurements are in good agreement with the size of crystallites estimated using the Scherrer equation. Figures 6c and 6d, which show the particle size distribution histograms of pure/green Ni-doped biosynthesized hematite NPs calcined at 700 ºC, illustrate the average size of the particles.

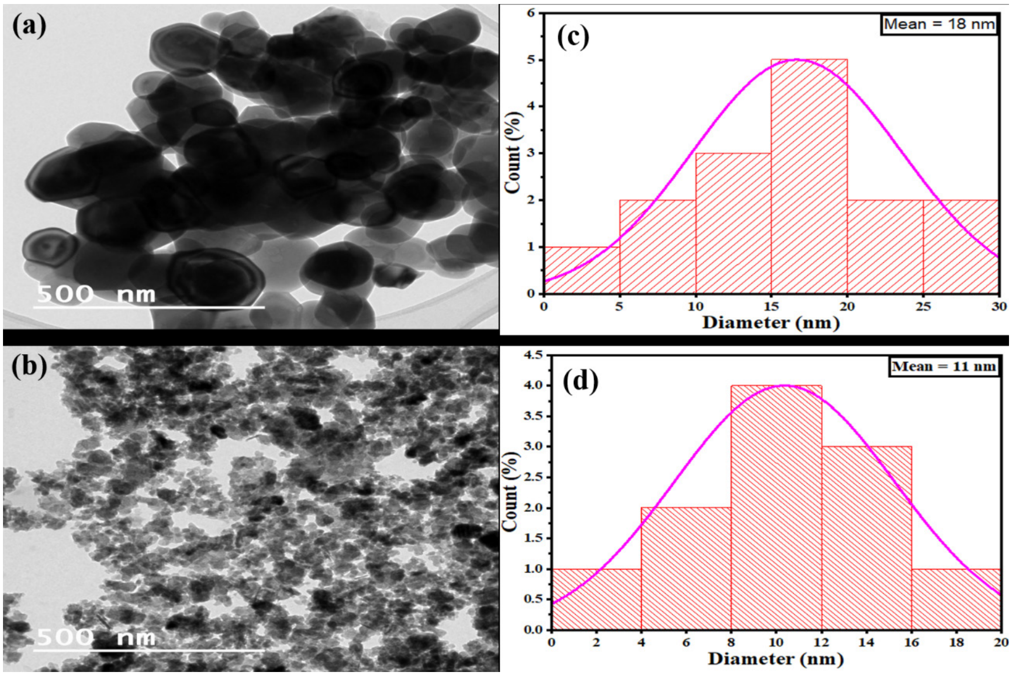

Figura 6. TEM & Histogram images of hematite crystal lattices of (a,c) Chemical Ni-doped hematite (α-Fe_2O_3) NPs and (b,d) Green Ni-doped hematite (α-Fe_2O_3) NPs.

3.6. Magnetic Properties Analysis

Using VSM at a temperature of 300 K and an external magnetic field varying between 15 kOe and +15 kOe, the magnetic characteristics of hematite and magnetite NPs were examined. The M-H hysteresis loop for the two samples is shown in Fig. 7 (a,b), and contains the measured value for saturation magnetization Ms (emu/g), coercivity Hc (Oe), and remanent magnetization Mr (emu/g) are enumerated in Table 4. The green Ni-doped hematite NPs have paramagnetic (exhibit near superparamagnetic) behaviour with a Ms value of 0.346 emu/g and the chemical Ni-doped hematite NPs have paramagnetic behaviour with a Ms value of 0.526 emu/g, according to the results of the hysteresis loop. Since no surfactant was used in this study, the elevated coercivity values for the hematite NPs samples may be partially attributed to a surface free of surfactants, or they may be caused by the existence of NPs aggregates that result in high coercivity values (Rafi, *et al.*, 2015; Liu, *et al.*, 2015). The growth of a saturated loop also supported the magnetic properties of both samples. Usually, morphology, particle size, and crystal structure are important determinants of a material’s magnetic properties (Mazrouaa, Mohamed, & Fekry 2019; Nguyen *et al.*, 2020).

Sample	Saturation magnetization (Ms) (emu/g)	Coercivity force (Hc) (Oe)	Remnant magnetization (Mr) (emu/g)	Remanence ratio (Mr/Ms)	Magnetic moment (μβ)
Chemical	0.3464	0.0990	0.09034	0.160	2.36
Green	0.5268	0.0382	0.07053	0.123	3.52

Table 4. Magnetic properties of chemical/green Ni doped hematite NPs.

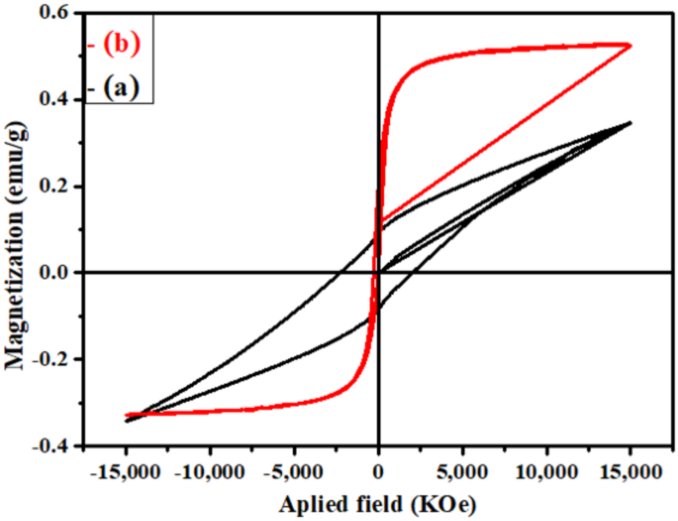

Figure 7. M-H curves for (a) Chemical Ni-doped hematite (α-Fe_2O_3) and (b) Green Ni-doped hematite (α-Fe_2O_3) NPs.

4. PHOTOCATALYTIC ACTIVITY

The ability of each sample of biosynthesized pure/green Ni-doped hematite NPs to degrade Malachite Green (MG) dye was assessed through UV light irradiation. The experiments were first carried out at pH = 12 with MG concentrations of 10, 15, and 20 mg/L and catalyst concentrations of 5, 10, and 15 mg with the pure/green hematite catalyst under UV-lamp irradiation, with other process conditions being held constant. MG highest absorbance peak was measured at 618 nm (Sukri, Isa, & Shameli, 2020; Bassi *et al.*, 2022). For all hematite-NPs samples and an influence study photocatalyst, the maximum absorption peak of MG is shown to gradually decline over time in Fig. 8. Additional adsorbent surfaces become available as the concentration of NPs rises, increasing the rate of reaction and causing the reaction to follow second-order kinetics (Singh *et al.*, 2020). Plachtova *et al.*, 2018 used zero-valent iron NPs to accomplish 93% dye decolorization in 100 ml of dye solution in 1 hour by increasing the pH to 9.0. Similar results were obtained by Sharma *et al.*, 2021, who raised pH to 8.3 and saw 93.75% dye decolorization in 2 hours. The intensity of absorption reduces to nearly zero in around 70 minutes of reaction time in the presence of pure/green Ni-doped hematite NPs photocatalyst, indicating a full degradation of MG dye for all samples, as indicated in Fig. (8 b-e). The MG degradation percentage (D%) was estimated using pseudo-first-order kinetics. Eq. (9-11) is used, and the result is displayed in either Table 5 or Fig. (8).

The rate constant was calculated using the following expression.

$$D(\%) = \frac{Co - Ct}{Co} \times 100 \tag{9}$$

The pseudo-first-order kinetic model

$$Ln\,(\,Ct\,/\,Co\,) = -K_{app}t \tag{10}$$

The half-life time of the dye degradation

$$t_{1/2} = 0.693\,/\,K_{app} \tag{11}$$

where D (%) is the degradation efficiency; Co is the initial MG concentration; Ct is the MG concentration at time t; and $t_{1/2}$ is the dye degradation half-life duration.

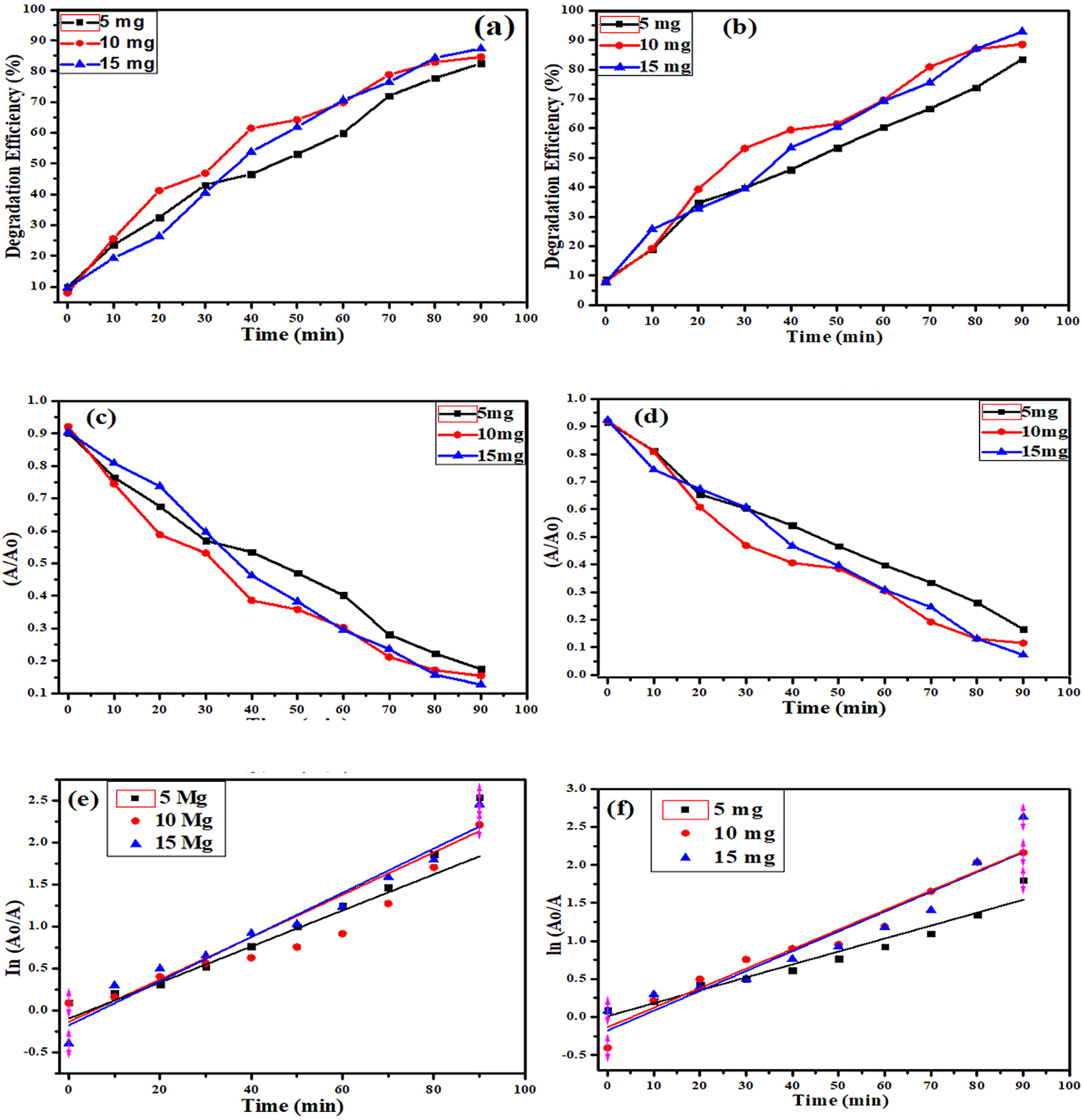

Figure 8. % degradation of chemical/green (a,b) the catalytic efficiency (c,d) and photodegradation kinetic (e,f) for MG dye Fe_2O_3 NPs

Method of Synthesis	Crystal Lattice	Concentrations (mg)	Degradation (%)	Rate constant (min^{-1})	Regression coefficient (R^2)
Chemical	Ni-Hematite	5	82	0.02525	0.93719
		10	84	0.02147	0.90501
		15	87	0.02632	0.95263
Green	Ni-Hematite	5	83	0.02605	0.94703
		10	88	0.01703	0.92084
		15	92	0.02968	0.98536

Table 5. Regression coefficient, rate constant, and percentage of degradation of chemically and green produced Ni-doped Fe_2O_3 NPs for MO dye.

According to Table 5, the degradation of MG dye similarly rises up to 92% as Fe_2O_3 NP concentration is increased from 5 to 15 mg. However, Ni-doped green hematite NPs degrade at a higher percentage than Ni-doped chemical hematite NPs. The capacity of synthesized NPs that provide active sites and excite electrons while exposed to ultraviolet radiation to induce photodegradation varies depending on their size, shape, and band gap.

4.1. Photocatalysis fundamental mechanism

Numerous researchers have explained and discussed the idea and process of photocatalysis. As an alternative or supplementary technology to the current water treatment process method, photocatalysis has lately come into existence. When catalytic semiconductor particles were exposed to UV light during photocatalysis, electron-hole pairs (e/h^+) were created (Koe, *et al.*, 2020; Regmi *et al.*, 2018; Saied, *et al.*, 2018). When exposed to visible light, electrons in the Valance band (VB) may be stimulated to the Covalent band (CB) of the oxide along with the corresponding production of holes, which results in the formation of an electron-hole pair. Redox reactions involving organic materials may then result from further electrostatic repulsion and the transfer of the created charge carriers towards the surface of the catalyst. Direct oxidation of MG to reactive compounds is made possible by the high oxidative potential of the hole (h^+) (VB) in the catalyst. The breakdown of water can also result in the formation of extremely reactive hydroxyl radicals (Fig. 9). The oxygen and hydroxyl radical, which is created when the produced electron and hole join with O^2 and H_2O to form, reacts with the dyes to break them down into nontoxic CO_2 and H_2O. Following is a description of the process's reactions:

$$Ni - (\alpha - Fe_2O_3) + hv \rightarrow Ni - (\alpha - Fe_2O_3) + e^- + h^+ \tag{12}$$

$$h^+ + MG \rightarrow MG^{\bullet +} \tag{13}$$

$$e^- + O_2^{\,o} \rightarrow O_2^{\bullet -} \tag{14}$$

$$h^+ + OH^- \rightarrow OH^\bullet \tag{15}$$

$$OH^\bullet + MG\ dye \rightarrow \text{intermediate product} \rightarrow H_2O + CO_2 \tag{16}$$

$$O_2^{\bullet -} + MG\ dye \rightarrow \text{intermediate product} \rightarrow H_2O + CO_2 \tag{17}$$

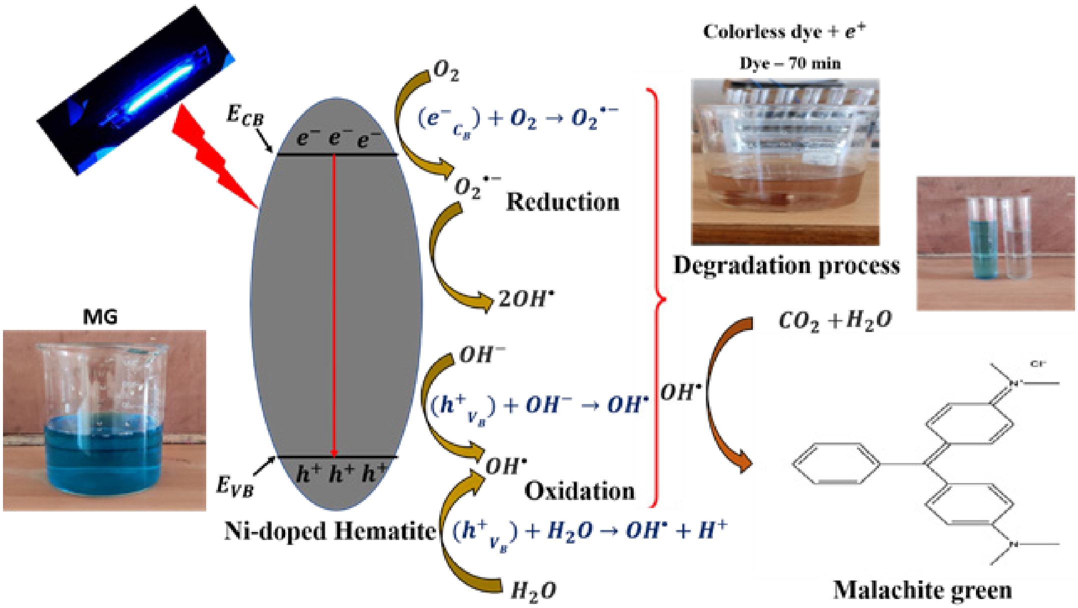

Figure 9. Schematic presentation of photocatalytic degradation mechanism utilizing Ni-doped hematite NPs under visible light irradiation.

5. CONCLUSION

Ni-doped hematite NPs have been successfully produced using co-precipitation with AI extract. The synthesis material was characterised using a variety of methods. Similar to this, XRD patterns and EDS elemental classifications confirmed that they were formed of uniformly distributed hematite NPs. Pure/green Ni-doped hematite NP samples are seen in the SEM and TEM to be agglomerated spherical in shape with reduced particle sizes. Raman spectroscopy was used to confirm hematite

NPs synthesis and identify its phonon modes: two A1g and five Eg. The FTIR analysis reveals the creation of chemical bonds, while the optical analysis reveals that the samples optical band gaps increased between 2.26 and 2.5 eV. Magnetic hysteresis loops revealed that the particles have high ferromagnetic order at ambient temperature. Furthermore, the degradation of MG dye was up to 82 and 92%, respectively, but green hematite NPs degraded faster than chemical hematite NPs. As a result, Ni-doped hematite NPs derived from widely available AI extract might be used to remediate organic dye-polluted water.

Acknowledgements

The authors are grateful to Centre for Nano-Science and Technology in Career Point University, Hamirpur (H.P.) for providing all the necessary facilities to conduct research work. In addition, the authors are grateful to Sophisticated Analytical Instrumentation Facility, Panjab University, Punjab and Sprint Testing Solutions, Mumbai for assistance of characterization of samples.

Conflict of Interest

The authors declare no competing financial interest. ◆

REFERENCES

Ahmed, S. F., Mofijur, M., Nuzhat, S., Chowdhury, A. T., Rafa, N., Uddin, M. A., Inayat, A., Mahlia, T. M. I., Ong, H. C., Chia, W. Y. and Show, P. L., 2021. Recent developments in physical, biological, chemical, and hybrid treatment techniques for removing emerging contaminants from wastewater. Journal of hazardous materials, 416, p. 125912.

Anu, Thakur, N., and Kumar, J., 2018. Synthesis and characterization of pure and Zn-doped copper oxide nanoparticles. International Journal of Advance Research in Science and Engineering, 7(8), pp. 1-5.

Anu, Thakur, N., Kumar, K. and Sharma, K. K., 2020. Application of Co-doped copper oxide nanoparticles against different multidrug resistance bacteria. Inorganic and Nano-Metal Chemistry, 50(10), pp. 933-943.

Balkrishna, A., Arya, V., Rohela, A., Kumar, A., Verma, R., Kumar, D., Nepovimova, E., Kuca, K., Thakur, N., Thakur, N. and Kumar, P., 2021a. Nanotechnology Interventions in the Management of COVID-19: Prevention, Diagnosis and Virus-Like Particle Vaccines. Vaccines, 9(10), p. 1129.

Balkrishna, A., Kumar, A., Arya, V., Rohela, A., Verma, R., Nepovimova, E., Krejcar, O., Kumar, D., Thakur, N. and Kuca, K., 2021b. Phytoantioxidant Functionalized Nanoparticles: A Green Approach to Combat Nanoparticle-Induced Oxidative Stress. Oxidative medicine and cellular longevity, 2021, pp. 1-20.

Cheng, Y., Ding, Y., Chen, J., Xu, W., Wang, W. and Xu, S., 2022. Au nanoparticles decorated covalent organic framework composite for SERS analyses of malachite green and thiram residues in foods. Spectrochimica Acta Part A: Molecular and Biomolecular Spectroscopy, 281, p. 121644.

Grabsi, I., Bouaïcha, F., Ziouche, A., Bouaziz, N., Zaabat, M. and Yildiz, F., 2022. Effect of Cobalt and Nickel Doping on Structural and Magnetic Properties of Iron Oxide Nanoparticles. Journal of Inorganic and Organometallic Polymers and Materials, 32(4), pp. 1287-1294.

Khatana, C., Kumar, A., Alruways, M. W., Khan, N., Thakur, N., Kumar, D., and Kumari, A., 2021. Antibacterial Potential of Zinc Oxide Nanoparticles Synthesized using Aloe vera (L.) Burm. f.: A Green Approach to Combat Drug Resistance. Journal of Pure and Applied Microbiology, 15(4), pp. 1907-1914.

Koe, W. S., Lee, J. W., Chong, W. C., Pang, Y. L. and Sim, L. C., 2020. An overview of photocatalytic degradation: photocatalysts, mechanisms, and development of photocatalytic membrane. Environmental Science and Pollution Research, 27(3), pp. 2522-2565.

Kumar, A., Ahmad, S., Chandel, T. and Thakur, N., 2021. Prediction of Intrinsic Spin Half-Metallicity and Ferromagnetism of Co-based Full Heusler Alloys: Hunt for Spintronic Applicability. DAE Solid State Physics Symposium, 55, pp. 581-582.

Kumar, A., Chandel, T., Diwaker and Thakur, N., 2020a. Predicting the magnetism, structural, thermodynamic and electronic properties of new co-based Heuslers: first principle perspective. Philosophical Magazine, 100(21), pp. 2721-2734.

Kumar, A., Singh, S., Sofi, S. A., Chandel, T. and Thakur, N., 2022b. Robustness in half-metallicity, thermophysical and structural properties of Co2YAl (Y= Pd, Ag) Heuslers: a first-principles perspective. Molecular Physics, 120(18), p. 2120839.

Kumar, A., Sofi, S. A., Chandel, T. and Thakur, N., 2023a. First-principles calculations to investigate structural stability, half-metallic behavior, thermophysical and thermoelectric properties of Co2YAl (Y= Mo, Tc) full Heusler compounds. Computational and Theoretical Chemistry, 1219, p. 113943.

Kumar, A., Thakur, N. and Chandel, T., 2020b. Tuning of electronic energy levels of NH3 passivated ZnO nanoclusters: A first principle study. Computational and Theoretical Chemistry, 1176, p. 112743.

Kumar, P., Thakur, N., Kumar, K. and Jeet, K., 2023b. Photodegradation of methyl orange dye by using Azadirachta indica and chemically mediated synthesized cobalt doped α-Fe2O3 NPs through co-precipitation method. Materials Today: Proceedings.

Lalitha, A., Subbaiya, R. and Ponmurugan, P., 2013. Green synthesis of silver nanoparticles from leaf extract Azhadirachta indica and to study its anti-bacterial and antioxidant property. Int J Curr Microbiol App Sci, 2(6), pp. 228-235.

Liu, X. D., Chen, H., Liu, S. S., Ye, L. Q. and Li, Y. P., 2015. Hydrothermal synthesis of superparamagnetic Fe3O4 nanoparticles with ionic liquids as stabilizer. Materials Research Bulletin, 62, pp. 217-221.

Patial, B. and Thakur, N., 2018. Green synthesis of silver nanoparticles using different plants. CPUH-Research Journal, 3(2), pp. 40-43.

Plachtová, P., Medrikova, Z., Zboril, R., Tucek, J., Varma, R. S. and Maršálek, B., 2018. Iron and iron oxide nanoparticles synthesized with green tea extract: differences in ecotoxicological profile and ability to degrade malachite green. ACS sustainable chemistry & engineering, 6(7), pp. 8679-8687.

Pradhan, G. K., Reddy, K. H. and Parida, K. M., 2014. Facile fabrication of mesoporous α-Fe2O3/SnO2 nanoheterostructure for photocatalytic degradation of malachite green. Catalysis Today, 224, pp. 171-179.

Regmi, C., Joshi, B., Ray, S. K., Gyawali, G. and Pandey, R. P., 2018. Understanding mechanism of photocatalytic microbial decontamination of environmental wastewater. Frontiers in Chemistry, 6, p. 33.

Sharma, S. and Kumar, K., 2021a. Aloe-vera leaf extract as a green agent for the synthesis of CuO nanoparticles inactivating bacterial pathogens and dye. Journal of Dispersion Science and Technology, 42(13), pp. 1950-1962.

Sharma, S., Kumar, K. and Thakur, N., 2021b. Green synthesis of silver nanoparticles and evaluation of their anti-bacterial activities: use of Aloe barbadensis miller and Ocimum tenuiflorum leaf extracts. Nanofabrication, 6(1), pp. 52-67.

Sharma, S., Kumar, K., Thakur, N. and Chauhan, M. S., 2020a. Ocimum tenuiflorum leaf extract as a green mediator for the synthesis of ZnO nanocapsules inactivating bacterial pathogens. Chemical Papers, 74(10), pp. 3431-3444.

Sharma, S., Kumar, K., Thakur, N., Chauhan, S. and Chauhan, M. S., 2020a. The effect of shape and size of ZnO nanoparticles on their antimicrobial and photocatalytic activities: a green approach. Bulletin of Materials Science, 43(1), pp. 1-10.

Sharma, S., Kumar, K., Thakur, N., Chauhan, S. and Chauhan, M. S., 2020b. The effect of shape and size of ZnO nanoparticles on their antimicrobial and photocatalytic activities: a green approach. Bulletin of Materials Science, 43(1), pp. 1-10.

Sharma, S., Kumar, K., Thakur, N., Chauhan, S. and Chauhan, M. S., 2021c. Eco-friendly Ocimum tenuiflorum green route synthesis of CuO nanoparticles: Characterizations on photocatalytic and antibacterial activities. Journal of Environmental Chemical Engineering, 9(4), p. 105395.

Sogut, E. G., Emre, D., Bilici, A., Kilic, N. C. and Yilmaz, S., 2022. Porous graphitic carbon nitride nanosheets coated with polyfluorene for removal of Malachite green and Methylene blue dyes and Cu (II) ions. Materials Chemistry and Physics, 290, p. 126523.

Testa-Anta, M., Ramos-Docampo, M. A., Comesaña-Hermo, M., Rivas-Murias, B. and Salgueiriño, V., 2019. Raman spectroscopy to unravel the magnetic properties of iron oxide nanocrystals for bio-related applications. Nanoscale Advances, 1(6), pp. 2086-2103.

Thakur, N., Anu and Kumar, K., 2020. Effect of (Ag, Co) co-doping on the structural and antibacterial efficiency of CuO nanoparticles: A rapid microwave assisted method. Journal of Environmental Chemical Engineering, 8(4), p. 104011.

Thakur, N., Kumar, K. and Kumar, A., 2021a. Effect of (Ag, Zn) co-doping on structural, optical and bactericidal properties of CuO nanoparticles synthesized by a microwave-assisted method. Dalton Transactions, 50(18), pp. 6188-6203.

Thakur, N., Kumar, K., Thakur, V. K., Soni, S., Kumar, A. and Samant, S. S., 2022a. Antibacterial and photocatalytic activity of undoped and (Ag, Fe) co-doped CuO nanoparticles via microwave-assisted method. Nanofabrication, 7, pp. 1-27.

Thakur, N., Thakur, N. and Kumar, K., 2023b. Phytochemically and PVP stabilized TiO2 nanospheres for enhanced photocatalytic and antioxidant efficiency. Materials Today Communications, 35, p. 105587.

Thakur, N., Thakur, N., Bhullar, V., Sharma, S., Mahajan, A., Kumar, K., Sharma, D. P. and Pathak, D., 2021b. TiO2 nanofibers fabricated by electrospinning technique and degradation of MO dye under UV light. Zeitschrift für Kristallographie-Crystalline Materials, 236(8-10), pp. 239-250.

Thakur, N., Thakur, N., Chauhan, P., Sharma, D. P., Kumar, A. and Jeet, K., 2022. Futuristic role of nanoparticles for treatment of COVID-19. Biomaterials and Polymers Horizon, 1(2), pp. 1-22.

Thakur, N., Thakur, N., Kumar, K. and Kumar, A., 2023a. Tinospora cordifolia mediated eco-friendly synthesis of Cobalt doped TiO2 NPs for degradation of organic methylene blue dye. Materials Today: Proceedings.

Yakasai, F., Jaafar, M. Z., Bandyopadhyay, S., Agi, A. and Sidek, M. A., 2022. Application of iron oxide nanoparticles in oil recovery–A critical review of the properties, formulation, recent advances and prospects. Journal of Petroleum Science and Engineering, 208, p. 109438.

* * *